Steam oxidation of Cr-coated Sn-containing Zircaloy solid rod at 1000 °C

Junkai Liu [a,b], Zhexin Cui [a], Zhe Hao [a], Dayan Ma [c], Junqiang Lu [d], Yanguang Cui [d], Chong Li [d], Wenbo Liu [a], Shijing Xie [a], Pengfei Hu [e], Ping Huang [c], Guanghai Bai [f], Di Yun [a,*]

[a] *School of Nuclear Science and Technology, Xi'an Jiaotong University, Xi'an, 710049, China*
[b] *Institute for Applied Materials (IAM), Karlsruhe Institute of Technology (KIT), D-76021, Karlsruhe, Germany*
[c] *State-key Lab for Mechanical Behavior of Materials, Xi'an Jiaotong University, Xi'an, 710049, China*
[d] *Shanghai Nuclear Engineering Research & Design Institute, Shanghai, 200233, China*
[e] *Institute of Materials, Shanghai University, Shanghai, 200072, China*
[f] *Suzhou Nuclear Power Research Institute, Suzhou, 215004, China*

ABSTRACT

In this study, the steam oxidation behavior of Cr-coated Zry-4 alloy at 1000 °C and the various interesting phenomena observed during the oxidation process were investigated. During oxidation, Sn in the Zry-4 substrate diffused into the coating and precipitated in the Cr_2O_3 scale. The Kirkendall effect of these Sn-containing precipitates then generated microcavities. Furthermore, the outward diffusion behavior of Zr and the selective oxidation mechanism of the Zr particles were studied. Voids detected at the Cr_2O_3/Cr interface result mainly from vacancy condensation. The amorphization of Cr_2O_3 was also observed adjacent to the voids, and the amorphization mechanism was discussed.

1. Introduction

Since the Fukushima nuclear power plant accidents in 2011, accident-tolerant fuel (ATF) has been globally researched and developed as a new kind of nuclear fuel to deal with loss-of-coolant accident (LOCA) in the nuclear industry [1–3]. In existing ATF concepts, the Zircaloy substrate with a surface protective coating is considered to be one of the most promising ATF candidate materials for industrial applications owing to the retention of commercial Zircaloy, the existing well-developed coating industry, and extensive research on coatings in other fields. It is cost effective and requires relatively less research and development time [1–3]. Recently, numerous types of coatings have been proposed by various researchers, including metallic coatings [5–9], oxide coatings [10,11], nitride coatings [12,13], and MAX phase coatings [14,15]. Among these coatings, Cr-metal coating is considered the most feasible choice for Zircaloy substrates. Moreover, it is potentially applicable in nuclear reactors because of its excellent corrosion and oxidation resistance, outstanding thermo-mechanical properties at high temperatures, favorable adhesion with Zircaloy substrate, capable irradiation resistance, and good neutron economy [4]. To date, several researchers have comprehensively studied different coating deposition techniques and the resulting microstructures [16,17], the mechanical

properties at both room temperature and high temperatures [17,18], the oxidation behavior in high-temperature steam [8,16,19], the corrosion resistance under reactor operating conditions [16], the performance under ion and neutron irradiations [20,21], and the performance in LOCA [18]. The steam oxidation behavior at high temperatures has become one of the most important factors in the performance evaluation of ATF candidate materials during accident scenarios.

Although the steam oxidation behavior of Cr-coated Zircaloy has been extensively studied, certain phenomena that can significantly affect the performance of Cr coatings have not garnered much attention. Firstly, the microstructural evolution of the oxide/metal (O/M) interface inside the Cr coating during steam oxidation was rarely investigated. During the high-temperature oxidation of Cr-containing alloys [22,23], the formation of voids at the interface between the Cr_2O_3 scale and the alloy matrix considerably affects the integrity of the dense and protective outer oxide scale and results in the loss of oxidation resistance. Numerous studies have reported the existence of this type of interface void during the high-temperature steam oxidation of Cr coatings on Zircaloy substrates [6,24], but the formation mechanism, microstructural evolution, and further effects of these voids on the coating microstructure and performance have yet to be clearly examined. Secondly, there are a few in-depth discussions about the selective oxidation

behavior of Zr inside the Cr coating, where the experiments indicated the outward diffusion of Zr into the Cr coating layer at high temperature even in the absence of an oxidative environment [25] and the formation of ZrO_2 grains (particles) at the grain boundaries of unoxidized Cr coating during oxidation [6,19]. These ZrO_2 grains can provide inward diffusion paths for oxygen and are considered detrimental to the oxidation resistance of the Cr coating layer. However, the oxidation mechanism of these Zr particles has rarely been discussed. The effects of ZrO_2 grains on the oxidation of Cr coating require further analysis because Zr is a reactive element and can greatly enhance the oxidation resistance of Cr. Finally, the influence of the alloying elements of Zircaloy on the oxidation performance of Cr coating has seldom been studied. Various studies examined the outward diffusion of Fe in the Zircaloy substrate and reported that the reaction involving Fe, Zr, and Cr resulted in the formation of $Zr(Cr, Fe)_2$ laves phase at the coating/substrate (C/S) interface [6,26,27]. Other alloying elements such as Sn can also be found in the commercial ZIRLO and Zircaloy-4 (Zry-4) alloys. It was reported that Sn precipitates at the ZrO_2 grain boundaries [28] and forms a "tin line" in the oxide layer parallel to the O/M interface [29] during the high-temperature steam oxidation of Sn-containing Zircaloy. This precipitation of Sn at the grain boundaries of ZrO_2 influences the oxidation behavior of Zircaloy and the "tin line" can enhance crack propagation in the oxide scale [29,30]. Therefore, the effect of these elements, especially Sn, on the steam oxidation behavior of Cr coatings requires further evaluation.

Herein, a Cr coating was deposited on commercial Zry-4 solid rods via vacuum cathodic arc ion plating. Thermogravimetric analyzer (TGA), X-ray diffraction (XRD), scanning electron microscope (SEM), transmission electron microscope (TEM), and energy-dispersive X-ray spectrometry (EDS), which is equipped within the SEM and TEM system, were used to study the steam oxidation behavior of the surface Cr coating at 1000 °C. The microstructural evolution of the C/S interface and the O/M interface inside the coating, the selective oxidation mechanism of Zr in the Cr coating, and the effect of Sn on the oxidation behavior of the Cr coating were given particular attention. Additional details were provided to comprehensively understand the performance of Cr-coated Zircaloy in a steam environment and to improve the design and development of Cr coatings on Zircaloy substrates.

2. Experimental

The materials used in this experiment were commercial Zry-4 alloy (Zr-1Sn-0.2Fe-0.1Cr) solid rods with lengths and outer diameters of 15 and 9.5 mm, respectively. Two samples were used in the current experiments: one for microstructural characterization before oxidation; and another for steam oxidation test. The surface Cr coatings were deposited on all three surfaces of the samples through vacuum cathodic arc ion plating. To hang the samples in the vacuum chamber during coating deposition, threaded holes were drilled into the base of the samples. Before deposition, all Zircaloy samples were etched in a mixed acid solution (volume ratio: 10 % hydrofluoric acid + 30 % sulfuric acid + 30 % nitric acid + 30 % water) for approximately 30 s to remove the surface oxide layer and initially decrease the sample's surface roughness. Subsequently, the samples were ultrasonically cleaned in acetone and ethanol for 15 min continuously to remove the residual acid and other impurities on the surface. The cleaned samples were then dried in hot air. During the coating deposition, a Cr target with a purity higher than 99.99 % was used as the cathode. The vacuum was controlled at 1×10^{-4} Pa, while the temperature and arc current were 400 °C and 100 A, respectively.

A TGA (NETZSCH STA 449 F) was used to test the steam oxidation behavior of the bare as well as coated Zircaloy sample at high temperature. TGA can provide the in situ weight gain data during oxidation. The process conditions were regulated to correspond to an isothermal oxidation process: an oxidation time of 1 h and a steam temperature of 1000 °C. The sample was first placed inside a corundum crucible with

the drilled face down. It was then placed together with the crucible on the specimen holder of the TGA. So only the top surface and the cylindrical side of the rod were directly in contact with the steam atmosphere. The furnace temperature of the TGA was increased from 35 to 1000 °C at a heating rate of 5 °C /min before isothermal oxidation, and the samples were protected from oxidation by flowing argon gas (purity > 99.999 %, 70 mL/min flow rate). When the furnace temperature reached 1000 °C, a gas mixture containing steam (produced by a water vapor generator and preheated at 150 °C) and argon (170 mL/min) was introduced into the furnace. The mass flow rate of water vapor was 1.5 g/h. After steam oxidation, the furnace cooled down at a cooling rate of 10 °C/min, the flow of steam was stopped, and only argon gas was injected at a flow rate of 170 mL/min.

XRD (Bruker D8) was utilized to study the phases on the sample surface before and after the high-temperature steam oxidation. The 2θ angle range was 20–100° and the scanning step was 0.02°. The surface and cross-sectional microstructures of the Cr-coated samples before and after the oxidation were observed with a high-resolution field-emission SEM (Gemini SEM 500) equipped with an EDS. The first step in the procedure to prepare the cross-sectional samples for SEM involved inlaying the samples in resin. They were then ground with the final step 3000-grit SiC sandpaper, which was followed by continuous polishing with 1 and 0.06 μm polishing pastes until the sample surface was mirror smooth. Finally, the samples were ultrasonically cleaned in ethanol for 15 min. TEM (JEOL JEM-F200) was used to further analyze the microstructure of the coating after steam oxidation, and the TEM sample was prepared using a focused ion beam (FIB, Helios Nanolab 600i) system.

3. Results

3.1. Microstructural characteristics

The XRD pattern of the as-deposited Cr coating is shown in Fig. 1. The cubic Cr phase was identified in the as-deposited coating, and small peaks corresponding to the α-Zr substrate were observed. The surface and cross-sectional microstructures of the as-deposited coatings are illustrated in Fig. 2. As shown in Fig. 2(a) and (b), the coating surface was relatively smooth without cracks, but had particles and defects distributed on it. The grain size of the Cr coating was uneven: the smallest grain was ~171.3 nm, the largest grain was ~1.3 μm, and the average grain size was ~659.1 nm. The cross-sectional morphology (Fig. 2(c)) indicated that the Cr coating had a dense structure with uniform thickness (average thickness ~5.7 μm) and that there were no obvious pores or cracks inside the coating. In addition, the coating
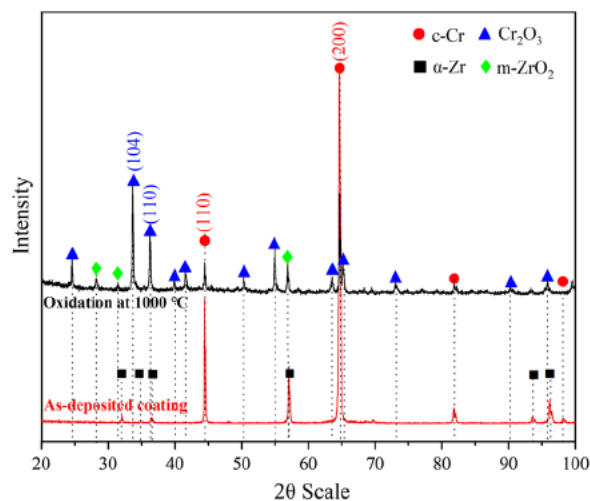
Fig. 1. X-ray diffraction patterns of the as-deposited Cr coating sample and the Cr-coated Zry-4 sample after steam oxidation at 1000 °C for 1 h.
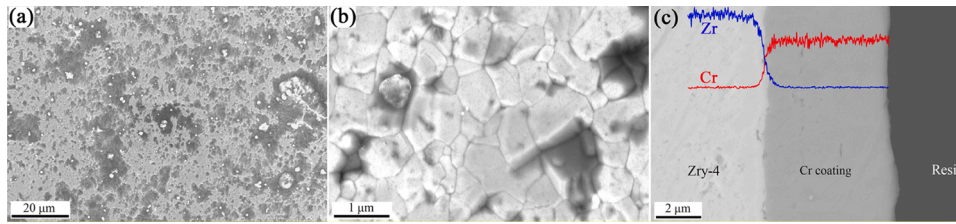
Fig. 2. Scanning electron microscope images of the as-deposited Cr coating on Zry-4 substrate: (a) surface morphology in low magnification; (b) surface morphology in high magnification; and (c) cross-sectional morphology together with energy-dispersive X-ray spectrometer line scans.

strongly adhered to the Zry-4 substrate and an interdiffusion layer was not detected at the C/S interface.

3.2. Steam oxidation tests

Fig. 3 shows the weight gain-time curve of the Cr-coated and bare Zry-4 samples during the 1 h steam oxidation at 1000 °C. The oxidation weight gain curve of bare Zry-4 follows parabolic kinetics, while an oxidation kinetics transition occurred at ~2000 s during the oxidation of the Cr-coated sample. After steam oxidation, the total weight gain of bare Zry-4 and Cr-coated Zry-4 were 1620.1 and 494.6 mg/dm^2, respectively. This oxidation kinetics transition and the large weight gain value of Cr-coated Zry-4 are mainly attributed to the extensive oxidation of the non-protected hole region at the bottom of the sample. To evaluate the fraction of mass change caused by the oxidation of Cr coating, a calculation was conducted based on the average thickness ~3.9 μm of the Cr$_2$O$_3$ scale in Fig. 4(c) after oxidation. A weight gain of 60.3 mg/dm^2 was obtained which is much smaller than the oxidation weight gain value of bare Zry-4. This implied that the surface Cr coating significantly improved the steam oxidation resistance of the Zry-4 alloy. Moreover, a weight gain curve was drawn in Fig. 3 based on the calculated weight gain value and the parabolic law, which was the actual oxidation kinetics law of Cr coating and was reported by other researchers [6]. The XRD pattern of the Cr-coated Zry-4 sample after oxidation (Fig. 1) demonstrated that the main oxidation product was Cr$_2$O$_3$, and the small peaks of c-Cr in the obtained pattern indicated that the coating was not totally consumed by oxidation. The appearance of the m-ZrO$_2$ phase and the kinetics transition were attributed to the formation of cracks in the edge region, which was due to the stress concentration and the low coating quality at the edge regions [12].

Fig. 4 illustrates the surface and cross-sectional morphologies of Cr-coated Zry-4 after oxidation at 1000 °C for 1 h. As seen in Fig. 4(a) and (b), the sample surface after oxidation was relatively dense and smooth,
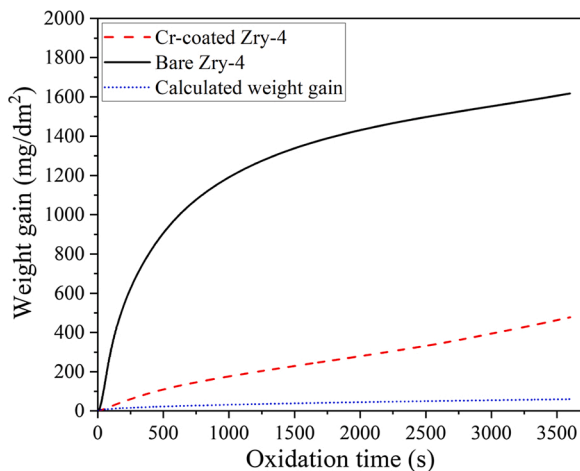
but particles were also detected on the surface. Moreover, the EDS line scans (Fig. 4(d)) and the EDS maps (Fig. 4(e)) showed that the unoxidized Cr coating layer remained after the steam oxidation process. As shown in Fig. 4(c), a dense and protective oxide scale developed on the surface of the coating, and the structural integrity of the coating has been preserved. The Zry-4 substrate was well-protected by the coating, which hindered the oxidation of the substrate. An α-Zr (O) layer formed beneath the surface coating (Fig. 4(c)), and the concentration of oxygen in α-Zr (O) layer was ~20 at.% studied by EDS. Nonetheless, the thickness of the outer oxide scale was non-uniform and a void layer was observed at the O/M interface of the coating (Fig. 4(c) and (d)). It must be emphasized that the appearance of voids at the O/M interface of the sample is a universal phenomenon and that the voids connected to each other promote the formation of cracks in local regions. Interestingly, when there were no voids at the O/M interface (within the red circle in Fig. 4(f)), the oxide scale was much thicker than that when voids were present at the interface. The EDS line scans (Fig. 4(d)) and the EDS maps (Fig. 4(e)) showed that a Cr–Zr interdiffusion layer with a thickness of ~1 μm formed at the C/S interface, and several researchers have thoroughly studied and identified this layer as ZrCr$_2$ [6,19]. Consequently, based on the EDS results, O and Zr were distributed in the unoxidized Cr coating layer.

3.3. TEM characterization

Fig. 5 displays the TEM characterization of the Cr-coated Zry-4 after steam oxidation. The TEM specimen was prepared using a FIB on the cross-section at the C/S interface. The TEM images revealed that there were four layers in the specimen, with each layer demarcated by a dashed line in the images (Fig. 5(a)). The phases of the four layers (Fig. 5(a); from outermost to innermost layer) were identified via EDS maps (Fig. 5(b)) and selected area electron diffraction (SAED, Fig. 5(c)). The outermost layer (f) is the Cr$_2$O$_3$ scale of the coating, while the following layer (e) is the unoxidized Cr coating layer. The ZrCr$_2$ intermetallic layer (d) can be attributed to the interdiffusion and solid-state reaction between the Cr coating and Zry-4 substrate, and the last layer (c) is α-Zr (O). The results showed that there are voids distributed at the O/M interface, which was consistent with the SEM characterization shown in Fig. 4. The EDS maps also indicated the following: 1) a large amount of Zr diffused into the Cr coating layer and was distributed along the grain boundaries of the Cr coating; 2) a small amount of Zr was distributed along the O/M interface; and 3) no Cr is observed in the α-Zr (O) substrate. Oxygen was present in the Cr$_2$O$_3$ layer and the concentration of oxygen in the Cr coating layer was high; however, only a diminutive amount of oxygen was found in the ZrCr$_2$ layer and substrate. The alloying element Fe underwent segregation in the ZrCr$_2$ layer, a phenomenon that was revealed and discussed in other studies [6,26,27].

3.3.1. The microstructure of oxide scale and precipitates

Fig. 6 demonstrates the microstructural characterization of the Cr$_2$O$_3$ layer. The scanning transmission electron microscope (STEM) micrograph (Fig. 6(a)) showed that the grains in the oxide layer were densely arranged and had an average grain size of 207.4 nm. Additionally, no large-size pores or voids were observed in the oxide layer. A large

Fig. 3. Weight gain vs. oxidation time of coated and uncoated samples in steam at 1000 °C for 1 h.
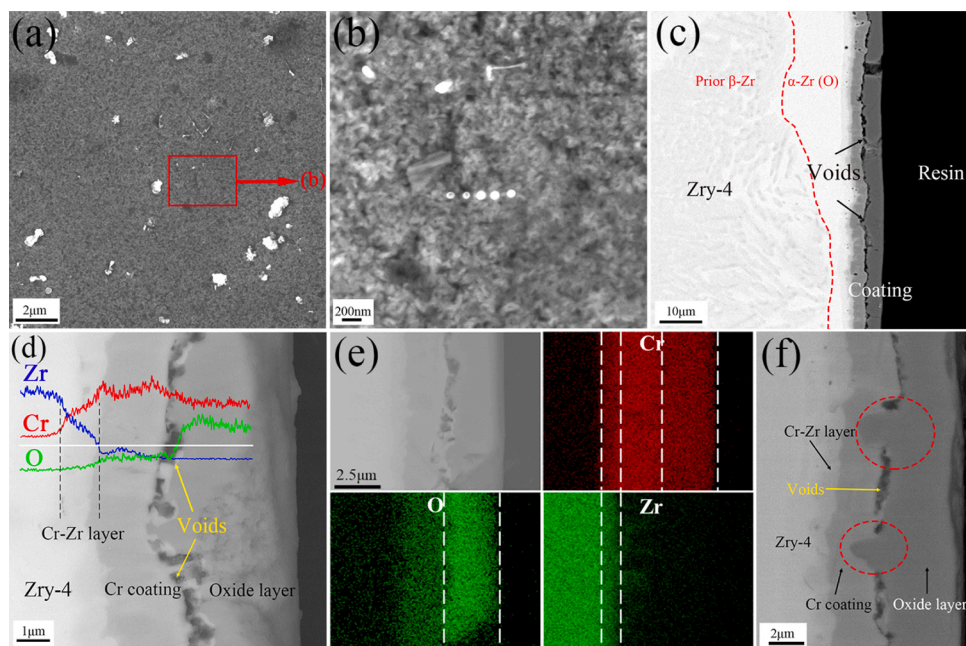
Fig. 4. Surface and cross-sectional morphologies of Cr-coated Zry-4 after oxidation at 1000 °C for 1 h: (a) surface morphology in low magnification; (b) surface morphology in high magnification; (c) cross-sectional morphology in low magnification; (d) cross-sectional morphology in high magnification together with energy-dispersive X-ray spectrometer (EDS) line scans; (e) EDS maps of cross-section; and (f) a typical scanning electron microscope image that shows the effect of voids on the oxidation of coating.
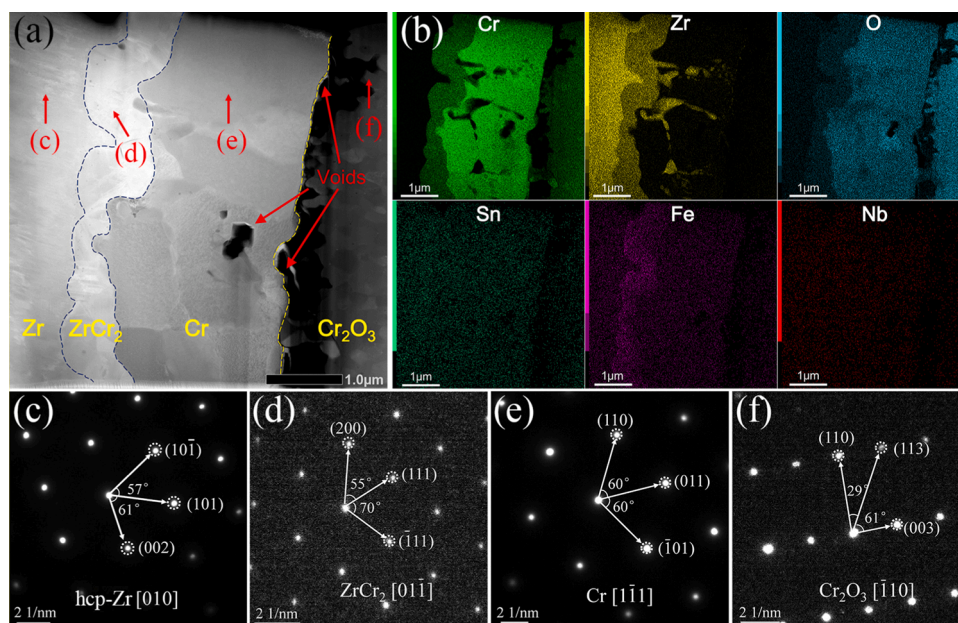
Fig. 5. Transmission electron microscope (TEM) characterization of the coating after steam oxidation at 1000 °C for 1 h: (a) Scanning TEM micrograph of the whole TEM specimen; (b) energy-dispersive X-ray spectrometer maps of the TEM specimen; and (c)–(f) selected area electron diffraction patterns of the four positions in (a).

number of white precipitates (denoted by yellow arrows) and black microcavities (denoted by blue arrows) were found inside the oxide grains and on the grain boundaries. Similarly, the higher magnification micrograph (Fig. 6(b)) showed that most of the white precipitates possessed microcavities (denoted by blue arrows) at the edge. According to the EDS maps illustrated in Fig. 6(c), only Sn segregation was observed inside the precipitates. The EDS point analyses of the six positions P1–P6 in Fig. 6(b) are listed in Table 1. The Sn concentrations measured at the positions of the two precipitates (P1 and P2) were significantly high, which was in good agreement with the EDS maps shown in Fig. 6(c). Conversely, almost no Sn was found in the Cr_2O_3 matrix (P5 and P6) and only a small amount of Sn was present inside both the microcavities (P3 and P4). Three types of precipitates with typical microstructures are displayed in Fig. 6(d), (f), and (g). The

precipitate shown in Fig. 6(d) is transgranular with a microcavity (blue circle) at the edge of the precipitate. Fig. 6(e) shows the high-resolution TEM (HRTEM) image of this precipitate, which indicates that the precipitate has a coherent lattice with the Cr_2O_3 matrix. The precipitate shown in Fig. 6(f) is at the triple junction and has a triangular shape, with its three corners pointing to the three grain boundaries. It was evident from the EDS line scans that there was a substantial variation in the amount of Sn in the precipitate. The precipitate illustrated in Fig. 6 (g) is also a transgranular Sn-containing precipitate, but the precipitate only exists at the edge of the microcavity.

The following theories were obtained when the distribution of microcavities and precipitates were analyzed: 1) individual microcavities are distributed only inside the Cr_2O_3 grains and they exist at the edge of precipitates at grain boundaries and 2) precipitates are mainly
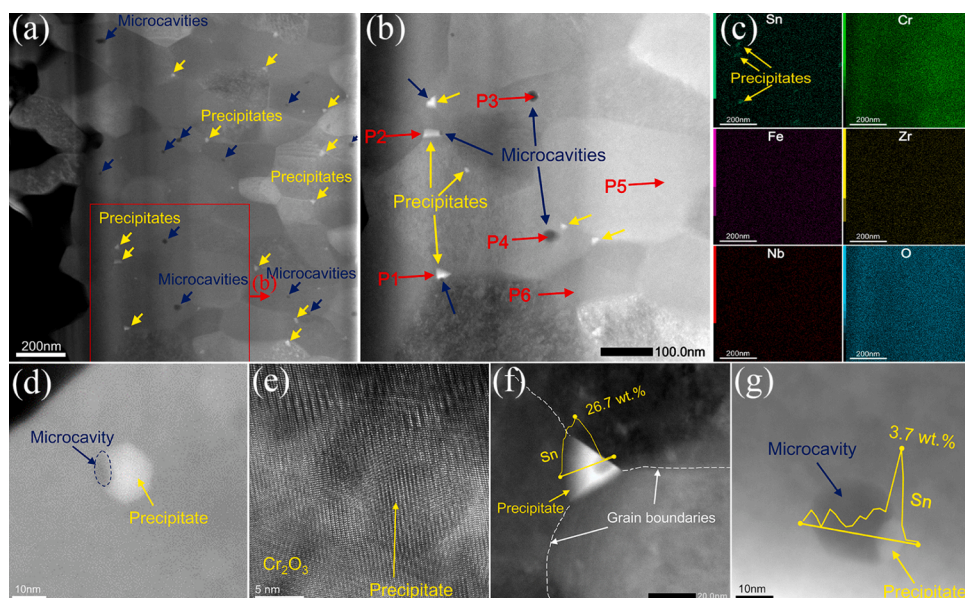
Fig. 6. Transmission electron microscope (TEM) characterization of the Cr_2O_3 layer: (a) Scanning TEM (STEM) micrograph of Cr_2O_3 layer in low magnification; (b) STEM micrograph of Cr_2O_3 layer in high magnification; (c) energy-dispersive X-ray spectrometer (EDS) maps of (b); (d) a Sn-containing precipitate with microcavity at edge; (e) High-resolution TEM micrograph of the precipitate in (d); (f) a Sn-containing precipitate at the triple junction together with EDS line scanning of Sn; (g) a microcavity with Sn precipitate at the edge together with EDS line scanning of Sn.

Table 1
Chemical compositions of the EDS point analyses in Fig. 6.

wt.%(at. %)	O	Cr	Fe	Zr	Nb	Sn
P1	31.3 (64.0)	48.0 (30.2)	0.5 (0.3)	/	/	20.2 (5.5)
P2	34.7 (65.7)	53.6 (31.2)	0.4 (0.2)	/	/	11.3 (2.9)
P3	36.1 (64.9)	62.6 (34.7)	0.4 (0.2)	/	/	0.9(0.2)
P4	37.9 (67.1)	58.0 (31.5)	0.8 (0.4)	2.1 (0.7)	0.7 (0.2)	0.5(0.1)
P5	44.5 (72.4)	54.0 (27.1)	0.4 (0.2)	1.1 (0.3)	/	/
P6	40.9 (69.4)	57.4 (30.0)	0.4 (0.2)	1.3 (0.4)	/	/

distributed at the Cr_2O_3 grain boundaries, and only a small amount of precipitates are present inside the grains. Four states of precipitates could be detected when the microstructure of the precipitates and microcavities were evaluated: 1) complete precipitates without any microcavities at the edge of the precipitates (Fig. 6(b)); 2) a microcavity appears at the edge of the precipitate, but the structure of the precipitate is intact (Fig. 6(d)); 3) a large part of the precipitate has become a microcavity, but a small amount of precipitate is present at the edge of the microcavity and is in contact with the Cr_2O_3 grains (Fig. 6(g)); and 4) complete microcavities without any precipitates (Fig. 6(b)). It is worth mentioning that microcavities randomly distributed on the edge of precipitates, and there is no relationship between the positions of microcavities and the diffusion direction of oxygen.

3.3.2. The microstructure of O/M interface in coating

Fig. 7 shows the microstructure of the O/M interface in the Cr coating. As can be seen in Fig. 7(a), a large number of voids are distributed at the O/M interface and an amorphous layer is present on the periphery of these voids. This layer was identified using the HRTEM image shown in Fig. 7(c) and the fast Fourier transform pattern (Fig. 7 (d)) of the HRTEM image. In addition, in the local region of the interface, oxide grains were closely connected to the Cr matrix and no voids were detected. It is worth noting that there is a certain correlation between the formation of voids and the appearance of an amorphous structure: the presence of amorphous regions always indicates the existence of voids at the inner O/M interface. In Fig. 7(b), a small grain can be seen at

the surface of the Cr matrix layer at position (e) within the void; this grain was identified as $m-ZrO_2$ via SAED (Fig. 7(e)). It is also worth mentioning that there were no grain boundaries in the inner Cr matrix beneath this ZrO_2 grain, which implied that this part of Zr diffused along the O/M interface from the intersections between the O/M interface and Cr grain boundaries. Inside the amorphous region, individual Cr_2O_3 crystal particles were observed at (f) and the relevant SAED pattern is shown in Fig. 7(f).

3.3.3. The microstructure of the unoxidized Cr coating and C/S interface

Fig. 8 shows the microstructure of the unoxidized Cr coating and the $ZrCr_2$ intermetallic compound layer. The average grain size of the Cr coating was measured as $\sim$1.6 μm, which indicates the grain size of Cr coating significantly increased at high temperature. The ZrO_2 grains distributed at the grain boundaries of the Cr coating can be seen in Fig. 8 (a). The concentration of the Zr particles in the Cr coating decreased gradually from the innermost to the outermost layer, but a small amount of Zr reached the O/M interface, as shown in Fig. 5(b). Fig. 8(b), (c), and (d) show the distribution of microcavities in the Cr metal, $ZrCr_2$, and Zr substrate, respectively. The EDS point analyses of the elemental contents inside the microcavities from P1 to P7 in Fig. 8(b) and (c) are listed in Table 2. P3, P4, and P7 are in the ZrO_2 grain, Cr layer, and $ZrCr_2$, respectively. There are no significant differences between the elemental contents present in the microcavities P1, P5, and P6 and the three types of matrices P3, P4, and P7. Microcavity P2 is special because its position is at the Cr/ZrO_2 interface. It can be seen from Fig. 8(d) that the Zr substrate and the $ZrCr_2$ layer close to the $ZrCr_2/Zr$ interface contain most of the microcavities, while inside of the Cr coating layer and the $ZrCr_2$ layer close to the $Cr/ZrCr_2$ interface possess only a few microcavities.

4. Discussion

4.1. The effects of Sn on the oxidation of Cr coating

Sn present inside the Cr_2O_3 layer must have diffused out of the Zircaloy substrate because Sn cannot be introduced during the coating deposition process. The outward diffusion of Sn to Cr coating occurred during the heating stage and the isothermal oxidation stage, and Sn mainly dissolved into the Cr coating because of the low content of Sn (1 wt.%) in the Zircaloy substrate and the high solubility of Sn in Cr (3.8 wt.% at 1000 °C according to the Cr-Sn phase diagram [31]). The
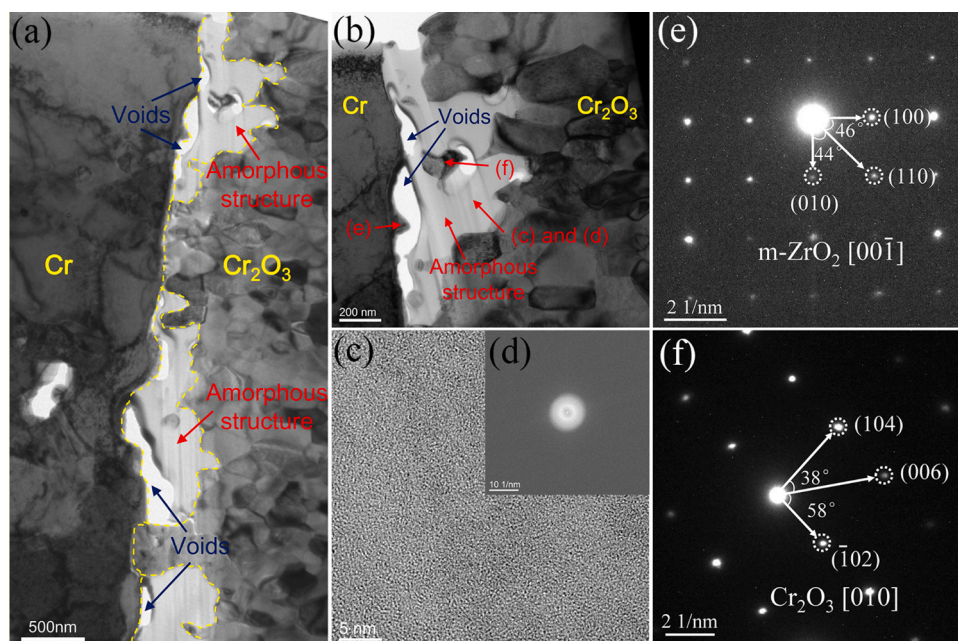
Fig. 7. Transmission electron microscope (TEM) characterization of the oxide/metal (O/M) interface of coating: (a) TEM micrograph of the O/M interface in low magnification; (b) TEM micrograph of the O/M interface in high magnification; (c) High-resolution TEM of the amorphous region at position (c) in (b); (d) the fast Fourier transform pattern of (c); (e) selected area electron diffraction (SAED) pattern of position (e) in (b); (f) SAED pattern of position (f) in (b).
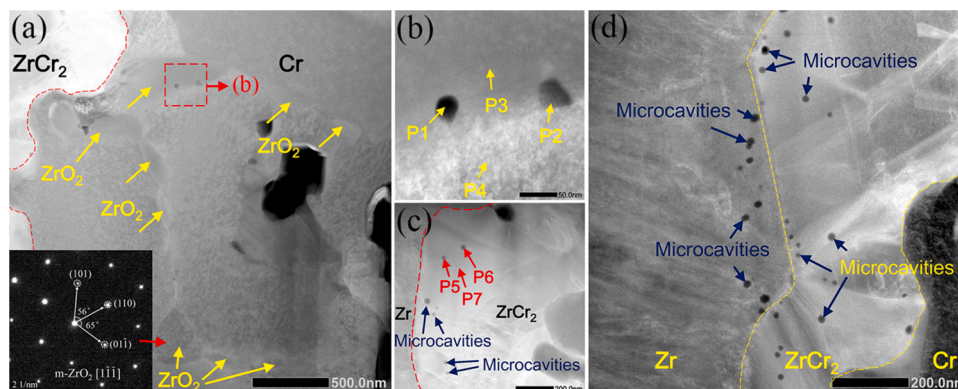
Fig. 8. (a) Scanning transmission electron microscope (STEM) micrograph of the Cr coating layer together with the selected area electron diffraction of ZrO_2 particle at Cr grain boundary; (b) STEM micrograph of the microcavities in Cr coating layer; (c) STEM micrograph of the $ZrCr_2$ layer; and (d) STEM micrograph of the microcavities close to the $ZrCr_2/Zr$ interface.

Table 2
Chemical compositions of the EDS point analyses in Fig. 8.

wt.%(at.%)	O	Cr	Fe	Zr	Nb	Sn
P1	11.4 (40.9)	6.1(6.8)	0.9 (0.9)	81.6 (51.4)	/	/
P2	7.7(29.0)	19.2 (22.3)	1.0 (1.1)	67.2 (44.5)	4.9 (3.1)	/
P3	12.9 (45.2)	1.9(2.0)	1.0 (1.0)	83.6 (51.5)	0.4 (0.2)	0.2 (0.1)
P4	/	97.2 (98.1)	0.9 (0.8)	1.5(0.9)	/	0.4 (0.2)
P5	0.3(1.2)	41.3 (53.8)	3.2 (4.0)	55.2 (41.0)	/	/
P6	0.5(2.0)	40.6 (52.9)	3.4 (4.2)	54.9 (40.6)	/	0.6 (0.3)
P7	0.3(1.1)	41.2 (53.8)	3.2 (3.9)	54.7 (40.8)	/	0.6 (0.4)

oxidation of Cr was triggered when steam was injected into the furnace and the dissolved Sn began to precipitate inside the Cr_2O_3 grains and at the Cr_2O_3 grain boundaries. Previous studies have also reported about the precipitation behavior of Sn in the oxide layer during the oxidation and corrosion of Sn-containing bare Zircaloy. Furthermore, these studies considered the phase state of Sn inside the ZrO_2 layer ambiguous and identified it as β-Sn [29], Sn-Zr intermetallic compounds [28], or oxides of Sn such as SnO and SnO_2 [32]. For the Cr-Sn system, because of the low eutectic temperature of Cr and β-Sn (~232 °C [31]), the Sn-containing precipitates were most likely to be either t-SnO_2, which is the stable oxide phase of Sn at high temperature [33], or Sn metal, which will be in the liquid phase at high temperatures and β-Sn at room temperature. It is evident that it is not yet possible to draw an accurate conclusion about the specific phase state of these precipitates even though there exists a coherent lattice relationship between the Sn-containing precipitate and hcp-Cr_2O_3 (Fig. 6(e)), thereby emphasizing the need for further precise characterization.

In accordance with the different morphologies of the precipitates inside the Cr_2O_3 grains and their relationship with the microcavities

(Fig. 6), a formation mechanism for the microcavities was proposed based on the Kirkendall effect, and the schematic is shown in Fig. 9. First, a Sn-containing precipitate with a perfect structure is present inside the Cr_2O_3 matrix, as shown in Fig. 9(a). Then, because of the difference between the diffusion coefficients of Sn and Cr, vacancies will diffuse into the precipitate and compensate for the diffusion flux during the interdiffusion of Cr and Sn. Hence, the microcavity nucleates inside the precipitate closest to the Cr_2O_3/precipitate interface through the coalescence of vacancies (Fig. 9(b)). When the microcavity formed, the diffusion of Sn along the free surface of the precipitate further accelerated the outward diffusion of Sn, causing the precipitate to become increasingly smaller, while the microcavity gradually grew by absorbing vacancies (Fig. 9(c)). Eventually, the precipitate completely transformed into a microcavity (Fig. 9(d)). It is important to note that there should be a thin $(Cr_{1-x}Sn_x)_2O_3$ layer around the microcavities; however, except for a small amount of Sn detected in the microcavities (Fig. 6(b)), this layer can hardly be observed because of its negligible thickness and low content of Sn. This kind of Kirkendall effect-surface diffusion behavior has been observed in other systems such as $SnO–Al_2O_3$ [34] and $CeO_2–ZrO_2$ [35] as well. The difference is that in this experiment, the microcavities inside the Cr_2O_3 grains can act as a vacancy sink for the absorption of cation vacancies that diffuse from the gas/oxide (G/O) interface to the O/M interface during the oxidation of Cr (Fig. 10(a)). Therefore, the microcavities could gradually grow and become larger than the original precipitate. Although the high-angle grain boundaries of Cr_2O_3 can act as effective sinks for vacancies [6], it is difficult to generate microcavities at the high-angle grain boundaries through nucleation and growth by vacancy condensation [36]. This is the reason why most of the Kirkendall microcavities had intragranular distribution. Nevertheless, the Kirkendall effect can occur at the grain boundaries, which was verified by the presence of small microcavities in the ridge region of the Sn-rich precipitates shown in Fig. 6(b).

The Sn-containing precipitates present inside the grains as well as at the grain boundaries influenced the performance of the Cr coating. The transgranular Sn-rich precipitates eventually led to the formation of microcavities because of the Kirkendall effect. These cavities will play the role of stress concentration point when stress is generated in the oxide and cause the oxide layer to fracture. Additionally, the precipitates at the grain boundaries have two types of impacts, and one among them is the reactive element effect (REE). The standard Gibbs formation energies (per mole of O_2) of ZrO_2, Cr_2O_3, SnO, and SnO_2 at 1000 °C were -858, -538, -318, and 317 kJ/mol [37], respectively. Compared with Cr, Sn does not have a strong affinity to oxygen, which implies that the Sn-rich precipitates at the grain boundaries of Cr_2O_3 can hardly act as the reactive element (RE) and is beneficial for the oxidation resistance of Cr. In fact, only a few studies have reported the circumstance that Sn acts as a RE to ameliorate the oxidation and corrosion behaviors of alloys. Lee et al. [28] reported that the Zr–Sn precipitates at the ZrO_2 grain boundaries are capable of inhibiting the diffusion of O, which will in turn enhance the oxidation resistance of the Zircaloy substrate. Nonetheless, there is no factual evidence for this inference. The second impact involves the stress generation due to Kirkendall effect. According to Klinger and Rabkin [38], a large stress will be generated when the Kirkendall effect occurs at the grain boundaries, and this stress will be

high enough to trigger intragranular fractures. Consequently, it can be surmised that the Sn-rich precipitates inside the coating will be detrimental to the integrity of the oxide layer, which will impact the performance of the coating under high-temperature steam.

4.2. The outward diffusion of Zr

The driving force for the outward diffusion of Zr is the oxygen potential gradient, which extends from the G/O interface to the substrate. According to studies on the interdiffusion behavior of Cr coating and Zircaloy substrate under argon atmosphere at high temperature [25], Zr can diffuse into the Cr coating and precipitate at the Cr grain boundaries even without oxidation or oxygen inward diffusion. Accordingly, this result indicated that the outward diffusion and precipitation of Zr began at the heating stage (without steam injection) in this experiment. These Zr precipitates were then oxidized into ZrO_2 possibly by the oxygen dissolved in the Cr coating or when steam was injected into the reaction furnace. The main reason for the preferential oxidation of Zr at the grain boundaries of the Cr coating layer is that Zr has a stronger affinity to oxygen than Cr (ZrO_2 has a lower standard Gibbs formation energy as mentioned in Section 4.1).

At the initial stages of steam oxidation, oxygen produced by steam decomposition can diffuse into the Cr coating layer through the thin outer oxide scale (or without oxide layer at the beginning of oxidation) and dissolve into the crystal lattice of Cr. With the inward diffusion of oxygen and outward diffusion of Zr, the oxygen activity at the Zr oxidation reaction front will reach the critical activity of nucleation of ZrO_2. Therefore, ZrO_2 begins to nucleate in the Zr crystal lattice adjacent to the Cr crystal, which was followed by the selective oxidation of Zr. As the reaction front moved forward, the Zr grains at the grain boundaries of Cr were gradually oxidized to ZrO_2, and this process preceded the oxidation of the Cr coating. Because the selective oxidation of Zr depends on the inward diffusion of oxygen, the Zr oxidation rate decreased with the increase in the thickness of the outer oxide scale, which could effectively inhibit the inward diffusion of oxygen. The selective oxidation of Zr hardly occurred in the $ZrCr_2$ intermetallic layer because of the negligible oxygen solubility in this layer [39]. As a result, the intermetallic layer was not attacked by oxygen or steam before the coating fracture or coating was completely oxidized.

Considering the effects of ZrO_2 at the grain boundaries of the Cr coating layer, Brachet et al. [6] suggested that the formation of a ZrO_2 layer and its influence in promoting the inward diffusion of oxygen lead to the oxidation kinetics transition of Cr-coated Zircaloy. In summary, Zr began to diffuse into the Cr coating layer at the heating stage before steam oxidation, the oxidation of the Zr precipitates was triggered by steam injection, and the oxidation rate decreased with time. These observations indicate that the influence of the selective oxidation of Zr on the oxidation weight gain of the Cr coating decreases as the steam oxidation progresses. Even if the ZrO_2 grains along the Cr grain boundaries provided oxygen diffusion paths, it would not significantly affect the oxidation behavior of the coating. This is because a minimum amount of oxygen can diffuse into the Cr coating through the dense Cr_2O_3 layer owing to the Cr oxidation mechanism that is based on cation outward diffusion and the much lower diffusion coefficient of oxygen
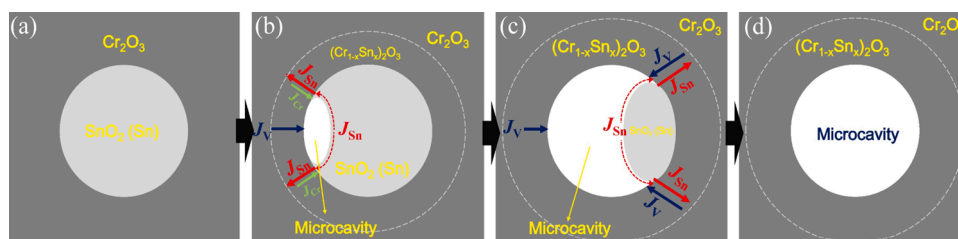
Fig. 9. The schematic of the formation of microcavities based on the Kirkendall effect of Sn-containing precipitates.
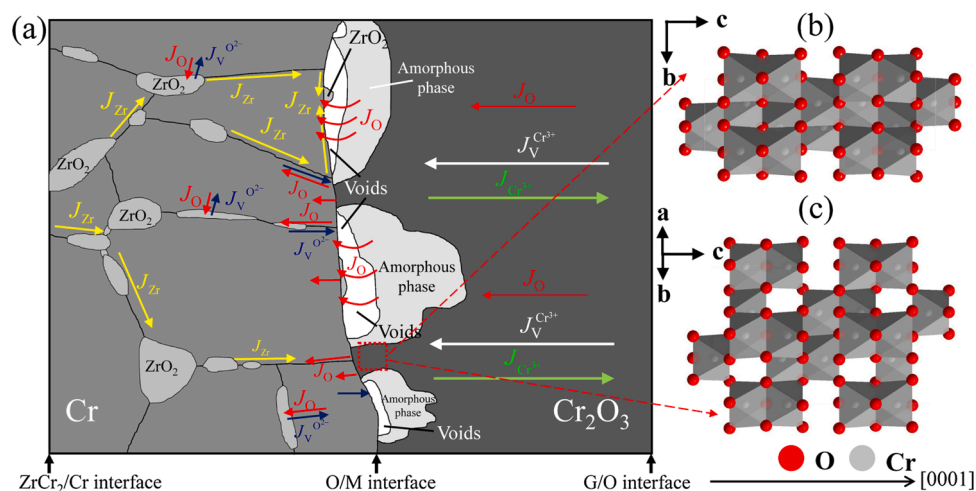
Fig. 10. (a) The schematic of elemental and vacancy diffusion behaviors in the oxide layer and Cr coating layer. The crystal structural schematics of hexagonal-Cr_2O_3 from the view along axis *a* (b) and towards (110) plane (c).

compared with that of Cr in the Cr_2O_3 layer [40,41].

Moreover, several studies have revealed that Zr can act as RE (such as Y, Ce, La, and Hf) and ameliorate the oxidation behavior when doped in the Cr metal or other materials [41–43]. Zr can only play the role of RE at a later stage when the O/M interface moves closer to the ZrO_2–containing Cr coating layer because of the limit outward diffusion distance of Zr in Cr coating from the substrate [25]. Owing to the REE of Zr, the outward short-circuit diffusion of cations can be inhibited by outward diffusion of Zr and ZrO_2 at Cr coating grain boundaries, thereby possibly reducing the oxidation rate and improving the oxidation resistance [23].

Therefore, it can be speculated that only when Zr diffuses into the Cr_2O_3 layer to form stable ZrO_2 particles at Cr_2O_3 grain boundaries or when the O/M interface moves forward and leaves stable ZrO_2 grains in the Cr_2O_3 layer can these ZrO_2 grains promote the inward diffusion of oxygen across the Cr_2O_3 layer [42] and destroy the protective dense structure of Cr_2O_3. It will further significantly affect the oxidation behavior of the coating. The formation of ZrO_2 grains along the whole thickness of the coating was observed and discussed in our another work [44]. In summary, only when the dense structure of the outer Cr_2O_3 layer is destroyed (mainly through the thickness decrease of Cr_2O_3 scale reported by Han et al. [45,46]) will the oxidation kinetics transition of the coating occur, even if ZrO_2 particles are present at the Cr grain boundaries.

The small cavities inside the Zircaloy substrate and the $ZrCr_2$ layer adjacent to the $ZrCr_2/Zr$ interface (Fig. 8(d)) were also detected in other studies [6,16], and the formation mechanism of these cavities was interpreted by Brachet [6]. Brachet stated that the larger diffusion co-efficient and higher solubility of Cr in β-Zr compared to that of Zr in Cr resulted in the formation of Kirkendall cavities. Nevertheless, several reports on Kirkendall cavities [34,35] and metal-metal solid-state re-actions [47,48] have shown that Kirkendall cavities invariably form at the side of the metal whose diffusion coefficient is larger and cavities are closest to the intermetallic layer. Based on this theory, the cavities should form inside the Cr coating layer or inside the $ZrCr_2$ layer closest to the $Cr/ZrCr_2$ interface, rather than inside the Zr substrate or closest to $Zr/ZrCr_2$ interface, which was discerned in the current Zircaloy sub-strate–Cr coating diffusion couples. Accordingly, the appearance of cavities on the substrate side suggested that the outward diffusion of the substrate was important in the interdiffusion behavior of the Zircaloy substrate and Cr coating, which was contrary to the diffusion coefficient data. Therefore, the interdiffusion behavior of the substrate and coating should be divided into two stages.

1) Early interdiffusion stage: The $ZrCr_2$ layer begins to form during this stage. Owing to the layer's thin nature, the inward diffusion of Cr was predominant here. The Kirkendall cavities formed in the Cr coating and $ZrCr_2$ layer were close to the $Cr/ZrCr_2$ interface. The remaining cavities are depicted in Fig. 8(a) and (b).

2) Later interdiffusion stage: In this stage, a thick $ZrCr_2$ layer and an α-Zr(O) layer beneath the $ZrCr_2$ layer were detected. The $ZrCr_2$ [49] and α-Zr(O) layers [25] significantly decreased the inward diffusion coefficient and solubility of Cr, respectively. In addition, the outward diffusion of Fe and Sn supplements the elemental mass flow from the substrate to the coating. Thus, Kirkendall cavities formed at the substrate and at the $ZrCr_2$ layer closest to the $Zr/ZrCr_2$ interface and resulted in the peculiar distribution of cavities observed in this experiment.

4.3. The formation of voids at the O/M interface

A large number of voids were observed at the O/M interface after steam oxidation. A number of studies have also reported the appearance of voids at the interface between the Cr_2O_3 scale and the unoxidized Cr coating during steam oxidation of Cr-coated Zircaloy [6,24]. The for-mation mechanism and the influence of voids present at the O/M interface in other kinds of metals [50] or alloys [22,42,51,52] during the oxidation process have been extensively examined. Moreover, interface voids are considered one of the most important factors that promote the reduction of adhesion between the oxide and metal, delamination of the oxide layer, breakaway oxidation behavior, and loss of oxidation resis-tance. The reasons for the generation of O/M interface voids can be divided into the following four categories: 1) the condensation of va-cancies at the interface [23,42,50,53]; 2) the internal oxidation of im-purities such as sulfur [23]; 3) Kirkendall effect during the oxidation of alloys that contain various elements with different diffusion coefficients [22,51]; and 4) the effect of hydrogen [54]. There are no sulfur impu-rities in commercial zirconium alloys [55] and the O/M interface cannot be easily influenced by hydrogen because of the excellent hydrogen barrier effect of the outer Cr_2O_3 [54,56]. Similarly, it is difficult for Kirkendall voids to develop when only a single Cr_2O_3 phase is generated during the oxidation process without interdiffusion behaviors with other cations inside the Cr coating. Therefore, vacancy condensation at the O/M interface is the only possibility.

The oxidation mechanism of Cr involves the outward diffusion of cations along the grain boundaries through the outer oxide layer and the formation of a new oxide layer at the G/O interface when the oxidation behavior is not affected by other factors such as REs. The reaction of the

oxide lattice growth at the G/O interface can be given by

$$\frac{3}{2}H_2O \rightarrow \frac{3}{2}O^2 + Cr_\square^3 + 3\dot{h} + \frac{3}{2}H_2 \tag{1}$$

where $Cr_\square^{3-}$ is a triply charged chromium ion vacancy and $\dot{h}$ is an electron hole. The reaction of the metal lattice consumption at the O/M interface can be given by

$$Cr + Cr_\square^3 + 3\dot{h} \rightarrow Cr^{3+} \tag{2}$$

During the process of oxidation, as shown in Fig. 10(a), cations diffused from the O/M interface into the external G/O interface and subsequently reacted with O ions to form oxides while cation vacancies are produced at the G/O interface and diffused into the O/M interface. When cation vacancies reach the O/M interface, three paths can be followed: 1) annihilation at the interface, as shown in Eq. 2 [57,58]; 2) vacancy injection in which the cation vacancies transform into metal vacancies and diffuse into the metal matrix [36,51]; and 3) condensation of voids at the interface [23,42,50,53]. In this experiment, the proportion of vacancy condensation and void formation at the O/M interface could be increased by the decrease of vacancy injection owing to the exhaustion of the vacancy sinks in the metal matrix [58], which occurred because of the oxidation of Zr at the grain boundaries of Cr and the outward diffusion of oxygen anion vacancies from ZrO2 to the Cr matrix (the process is shown in Fig. 10(a)). Additionally, oxygen anion vacancies produced by the oxidation of Zr diffused toward the O/M interface, which was beneficial for the formation of voids. As shown in Fig. 4(f), the interface voids can reduce the oxidation rate of the coating to a certain extent by inhibiting the outward diffusion of cations. The local oxygen activity and the oxygen partial pressure will increase with the outward migration of the cations present in the inner surface of the scale close to the voids [59]. Consequently, the evaporation of oxygen occurred in the inner oxide layer outside the voids due to the decomposition of Cr2O3 according to Eq. 3:

$$O^2 \rightarrow O_\square^{2+} + \frac{1}{2}O_2 + 2e \tag{3}$$

where $O_\square^{2+}$ is anion vacancy. The generated oxygen gas (Eq. 3) migrated inward through the interface voids and formed an oxide on the metal surface (Fig. 10(a)). If the inner Cr2O3 close to the O/M interface completely decomposed, leading to the formation of a porous oxide layer between the outer dense scale and the metal matrix, the reaction follows Eq. 4 shown below:

$$Cr_2O_3 \rightarrow \frac{3}{2}O_2 + 2Cr^{3+} + 6e \tag{4}$$

The decomposition of Cr2O3 in Eq. 4 produces oxygen, but it also provides cations and compensates for the outward diffusion of cations [59]. The oxidation mechanism of Cr was transformed from a cation outward diffusion to a combination of cation outward diffusion and oxygen inward diffusion by the interface voids. This supports the observation that a few pores formed inside the scale close to the O/M interface (interface voids), and thus, the formation of oxygen primarily followed Eq. 3 in this experiment. If voids coalesce with each other and eventually trigger scale buckling, the oxidation resistance of the coating will be destroyed and the oxide scale will undergo spallation during the high-temperature oxidation of Cr coating on Zircaloy's surface [16]. Nonetheless, it was observed that the inward diffusion of oxygen healed the interface voids [52]. Thus, new oxide grains formed at the interface and the voids were filled because of the volume expansion occurring (Pilling-Bedworth ratio (PBR) of Cr–Cr2O3 is ~2 [60]) during the process of oxidation. The tendency of the voids to heal was also observed in this experiment, which was demonstrated by the small ZrO2 grain detected on the metal surface beneath the voids (Fig. 7(b)). The inward diffusion of oxygen will also be inhibited when voids are formed, and as a result Zr diffused out from the substrate can hardly be oxidized at the

Cr grain boundaries. As shown in Fig. 10(a), Zr diffuses into the O/M interface and then diffuses along the interface toward the position of voids and reacts with oxygen. Considering the complex process of the void formation mechanism and its important effects on the oxidation behavior of the Cr coating, a comprehensive analysis of the interface void evolution behavior needs to be conducted in the future.

4.4. The amorphization of Cr2O3

The decomposition of Cr2O3 and the formation of oxygen vacancies through Eq. 3 could be the main reason for the amorphization of Cr2O3. The crystal structural schematics of hexagonal-Cr2O3 from the view along axis a and toward the (110) plane are shown in Fig. 10(b) and (c), respectively. In a unit cell of Cr2O3, the CrO6 octahedra are connected to each other by a mixture of corners (sharing one oxygen atom), edges (sharing two oxygen atoms), and faces (sharing three oxygen atoms) along the three axes. The positions of the oxygen vacancies formed during decomposition are precisely the positions of oxygen atoms that connect the CrO6 octahedra. Therefore, the formation of oxygen vacancies could lead to the disruption of the connectivity between octahedral and could further cause structural failure and order-disorder transformation of the Cr2O3 grains. This type of oxygen vacancy-induced amorphization was also reported in Ta2O5 [61] and mullite ceramic (3Al2O3·2SiO2) [62] under the action of stress. The difference is, the high temperature and the decomposition of Cr2O3 during the oxidation of Cr coating take the place of stress and become the source of oxygen vacancies. Amorphization will be beneficial for the oxidation resistance attributed to the disappearance of grain boundaries and will make further short-circuit diffusion of ions along the grain boundaries unfeasible [63]. The disordered structure of amorphous grains is beneficial for the release of stress on the scale, but the strength of the oxide layer will be affected.

5. Conclusions

The steam oxidation behavior of Cr-coated Sn-containing Zircaloy solid rod at 1000 °C for 1 h was studied in detail. Several interesting phenomena were observed throughout this experiment below:

(1) Sn-containing precipitates were distributed inside the Cr2O3 grains and at the Cr2O3 grain boundaries because of the outward diffusion of Sn from the Zircaloy substrate to the Cr coating layer and the precipitation during the oxidation of the Cr coating. Microcavities were also observed inside the Cr2O3 scale, and their distribution have a relationship with the precipitates. The formation of microcavities was due to the Kirkendall effect during the interdiffusion of Sn in precipitates and Cr in Cr2O3 grains.

(2) The Zr diffused outward to Cr coating along the grain boundaries of Cr, and was further oxidized by the dissolved oxygen in coating and the oxygen diffused from the G/O interface. The Zr/ZrO2 at the Cr grain boundaries could act as a RE and improve the oxidation resistance of the Cr coating.

(3) The interdiffusion of Zr and Cr at the C/S interface comprises two main stages according to the distribution of the Kirkendall cavities, which are close to the Zr/ZrCr2 interface. The inward diffusion of Cr controlled the early stage of diffusion, whereas in the later stage, a thick ZrCr2 layer and an α-Zr(O) layer were detected, which decreased the inward diffusion coefficient and solubility of Cr. As a result, the total outward mass flow of Zr, Fe, and Sn was much higher than the inward mass flow of Cr.

(4) Voids were observed at the O/M interface in the coating, and the formation mechanism of voids was attributed to the condensation of cation vacancies—that diffuse from the G/O interface to the O/M interface—and oxygen ion vacancies—that diffuse from ZrO2 particles in the Cr coating layer to the O/M interface—at the O/M interface. The interface voids transform the oxidation mechanism

of Cr and improve the oxidation resistance of the Cr coating to some extent but destroy the structural integrity of the coating and the adhesion between the oxide scale and Cr matrix.

(5) The Cr_2O_3 grains close to the O/M interface transformed into an amorphous structure because of the formation of oxygen vacancies during the decomposition of the Cr_2O_3 grains.

Author statement

Junkai Liu : Conceptualization, Methodology, Investigation, Writing - Original Draft.
Zhexin Cui: Investigation, Data Curation.
Zhe Hao : Writing - Review & Editing, Investigation.
Dayan Ma: Conceptualization, Resources, Writing - Review & Editing.
Junqiang Lu: Project administration, Resources.
Yanguang Cui : Visualization.
Chong Li : Conceptualization.
Wenbo Liu : Writing - Review & Editing, Methodology.
Shijing Xie: Writing - Review & Editing.
Pengfei Hu : Methodology, Investigation.
Ping Huang : Resources.
Guanghai Bai : Investigation, Conceptualization.
Di Yun: Writing - Review & Editing, Supervision, Project administration.

Data availability

The raw data required to reproduce these findings cannot be shared at this time as the data also forms part of an ongoing study. The processed data required to reproduce these findings cannot be shared at this time as the data also forms part of an ongoing study.

Declaration of Competing Interest

The authors declare that they have no known competing financial interests or personal relationships that could have appeared to influence the work reported in this paper.

Acknowledgements

References

[1] S.J. Zinkle, K.A. Terrani, J.C. Gehin, L.J. Ott, L.L. Snead, Accident tolerant fuels for LWRs: a perspective, J. Nucl. Mater. 448 (2014) 374–379.
[2] L.J. Ott, K.R. Robb, D. Wang, Preliminary assessment of accident-tolerant fuels on LWR performance during normal operation and under DB and BDB accident conditions, J. Nucl. Mater. 448 (2014) 520–533.
[3] J.K. Liu, X.H. Zhang, D. Yun, A complete review and a prospect on the candidate materials for accident-tolerant fuel claddings, Mater. Rev. 32 (2018) 1757–1778.
[4] C. Tang, M. Stueber, H.J. Seifert, M. Steinbrueck, Protective coatings on zirconium-based alloys as accident-tolerant fuel (ATF) claddings, Corros. Rev. 35 (2017) 141–165.
[5] J. Brachet, I. Idarraga-Trujillo, M.L. Flem, M.L. Saux, V. Vandenberghe, S. Urvoy, E. Rouesne, T. Guilbert, C. Toffolon-Masclet, M. Tupin, C. Phalippou, F. Lomello, F. Schuster, A. Billard, G. Velisa, C. Ducros, F. Sanchette, Early studies on Cr-Coated Zircaloy-4 as enhanced accident tolerant nuclear fuel claddings for light water reactors, J. Nucl. Mater. 517 (2019) 268–285.
[6] J. Brachet, E. Rouesne, J. Ribis, T. Guilbert, S. Urvoy, G. Nony, C. Toffolon-Masclet, M. Le Saux, N. Chaabane, H. Palancher, A. David, J. Bischoff, J. Augereau, E. Pouillier, High temperature steam oxidation of chromium-coated zirconium-based alloys: kinetics and process, Corros. Sci. 167 (2020), 108537.
[7] X. Han, C. Chen, Y. Tan, W. Feng, S. Peng, H. Zhang, A systematic study of the oxidation behavior of Cr coatings on Zry4 substrates in high temperature steam environment, Corros. Sci. 174 (2020), 108826.
[8] X. Han, Y. Wang, S. Peng, H. Zhang, Oxidation behavior of FeCrAl coated Zry-4 under high temperature steam environment, Corros. Sci. 149 (2019) 45–53.
[9] F.O. George, P. Skeldon, G.E. Thompson, Formation of zirconium-based conversion coatings on aluminium and Al–Cu alloys, Corros. Sci. 65 (2012) 231–237.
[10] G. Li, C. Cai, Y. Wang, Y. Zhou, L. Yang, J. Lu, G. Zhou, Zirconium silicate growth induced by the thermochemical interaction of yttria-stablized zirconia coatings with molten CMAS deposits, Corros. Sci. 149 (2019) 249–256.
[11] V. Malinovschi, A. Marin, D. Negrea, V. Andrei, E. Coaca, C.N. Mihailescu, C.P. Lungu, Characterization of Al 2 O 3 /ZrO 2 composite coatings deposited on Zr-2.5Nb alloy by plasma electrolytic oxidation, Appl. Surf. Sci. 451 (2018) 169–179.
[12] J. Liu, Z. Cui, D. Ma, J. Lu, Y. Cui, C. Li, W. Liu, Z. Hao, P. Hu, M. Yao, P. Huang, G. Bai, D. Yun, Investigation of oxidation behaviors of coated Zircaloy as accident-tolerant fuel with CrAlN and CrAlSiN coatings in high-temperature steam, Corros. Sci. 175 (2020), 108896.
[13] Z. Gao, Y. Chen, J. Kulczyk-Malecka, P. Kelly, Y. Zeng, X. Zhang, C. Li, H. Liu, N. Rohbeck, P. Xiao, Comparison of the oxidation behavior of a zirconium nitride coating in water vapor and air at high temperature, Corros. Sci. 138 (2018) 242–251.
[14] C. Tang, M. Steinbrueck, M. Stueber, M. Grosse, X. Yu, S. Ulrich, H.J. Seifert, Deposition, characterization and high-temperature steam oxidation behavior of single-phase Ti 2 AlC-coated Zircaloy-4, Corros. Sci. 135 (2018) 87–98.
[15] B.R. Maier, B.L. Garcia-Diaz, B. Hauch, L.C. Olson, R.L. Sindelar, K. Sridharan, Cold spray deposition of Ti2AlC coatings for improved nuclear fuel cladding, J. Nucl. Mater. 466 (2015) 712–717.
[16] T. Wei, R. Zhang, H. Yang, H. Liu, S. Qiu, Y. Wang, P. Du, K. He, X. Hu, C. Dong, Microstructure, corrosion resistance and oxidation behavior of Cr-coatings on Zircaloy-4 prepared by vacuum arc plasma deposition, Corros. Sci. 158 (2019), 108077.
[17] H. Kim, I. Kim, Y. Jung, D. Park, J. Park, Y. Koo, Adhesion property and high-temperature oxidation behavior of Cr-coated Zircaloy-4 cladding tube prepared by 3D laser coating, J. Nucl. Mater. 465 (2015) 531–539.
[18] J.C. Brachet, M. Dumerval, V. Lezaud-Chailioux, M. Le Saux, E. Rouesne, D. Hamon, S. Urvoy, T. Guilbert, Q. Houmaire, C. Cobac, Behavior of chromium coated M5TM claddings under LOCA conditions, WRFPM 2017 Water Reactor Fuel Performance Meeting. WRFPM 2017 Water Reactor Fuel Performance Meeting (2017).
[19] X. Han, C. Chen, Y. Tan, W. Feng, S. Peng, H. Zhang, A systematic study of the oxidation behavior of Cr coatings on Zry4 substrates in high temperature steam environment, Corros. Sci. 174 (2020), 108826.
[20] L.B. Begrambekov, A.E. Evsin, A.V. Grunin, A.I. Gumarov, A.S. Kaplevsky, N.F. Kashapov, A.G. Luchkin, I.R. Vakhitov, I.V. Yanilkin, L.R. Tagirov, Irradiation with hydrogen atoms and ions as an accelerated hydrogenation test of zirconium alloys and protective coatings, Int. J. Hydrogen Energ. 44 (2019) 17154–17162.
[21] A.S. Kuprin, V.A. Belous, V.N. Voyevodin, R.L. Vasilenko, V.D. Ovcharenko, G.D. Tolstolutskaya, I.E. Kopanets, I.V. Kolodiy, Irradiation resistance of vacuum arc chromium coatings for zirconium alloy fuel claddings, J. Nucl. Mater. 510 (2018) 163–167.
[22] D.L. Douglass, The oxidation mechanism of dilute Ni-Cr alloys, Corros. Sci. 8 (1968) 665–678.
[23] M. Li, P. Hou, Improved Cr2O3 adhesion by Ce ion implantation in the presence of interfacial sulfur segregation, Acta Mater. 55 (2007) 443–453.
[24] X. He, Z. Tian, B. Shi, X. Xu, C. Meng, W. Dang, J. Tan, X. Ma, Effect of gas pressure and bias potential on oxidation resistance of Cr coatings, Ann. Nucl. Energy. 132 (2019) 243–248.
[25] J. Yang, U. Stegmaier, C. Tang, M. Steinbrück, M. Große, S. Wang, H.J. Seifert, High temperature Cr-Zr interaction of two types of Cr-coated Zr alloys in inert gas environment, J. Nucl. Mater. 547 (2021), 152806.
[26] J. Ribis, A. Wu, J.C. Brachet, F. Barcelo, B. Arnal, Atomic-scale interface structure of a Cr-coated Zircaloy-4 material, J. Mater. Sci. 53 (2018) 9879–9895.
[27] A. Wu, J. Ribis, J.C. Brachet, E. Clouet, F. Leprêtre, E. Bordas, B. Arnal, HRTEM and chemical study of an ion-irradiated chromium/zircaloy-4 interface, J. Nucl. Mater. 504 (2018) 289–299.
[28] C.M. Lee, D. Sohn, Enhanced high-temperature oxidation resistance of a zirconium alloy cladding by high-temperature preformed oxide on the cladding, Corros. Sci. 131 (2018) 116–125.
[29] M. Grosse, R. Simon, Analysis of tin diffusion in Zircaloy-4 and tin redistribution after steam oxidation by means of X-ray fluorescence measurements, Adv. Eng. Mater. 11 (2009) 483–487.
[30] G.J. Yurek, J.V. Cathcart, R.E. Pawel, Microstructures of the scales formed on zircaloy-4 in steam at elevated temperatures, Oxid. Met. 10 (1976) 255–276.
[31] M. Venkatraman, J.P. Neumann, The Cr— Sn (Chromium-Tin) system, Journal of Phase Equilibria. 9 (1988) 159–162.
[32] H. Hulme, F. Baxter, R.P. Babu, M.A. Denecke, M. Gass, A. Steuwer, K. Norén, S. Carlson, M. Preuss, An X-ray absorption near-edge structure (XANES) study of the Sn L3 edge in zirconium alloy oxide films formed during autoclave corrosion, Corros. Sci. 105 (2016) 202–208.
[33] M. Huh, S. Kim, J. Ahn, J. Park, B. Kim, Oxidation of nanophase tin particles, Nanostructured Mater. 11 (1999) 211–220.
[34] H.J. Fan, M. Knez, R. Scholz, D. Hesse, M. Nielsch, M. Zacharias, U. Gosele, Influence of surface diffusion on the formation of hollow nanostructures induced by the kirkendall effect: the basic concept, Nano Lett. 7 (2007) 993–997.
[35] X. Liang, S. Wang, Y. Zhuang, B. Xu, S. Kuang, Y. Li, Formation of CeO2 −ZrO2 solid solution nanocages with controllable structures via kirkendall effect, J. Am. Chem. Soc. 130 (2008) 2736–2737.
[36] J.E. Harris, Vacancy injection during oxidation—a re-examination of the evidence, Acta Metall. 26 (1978) 1033–1041.

[37] I. Barin, Thermochemical Data of Pure Substances, VCH, 1989.

[38] L. Klinger, E. Rabkin, Theory of the Kirkendall effect during grain boundary interdiffusion, Acta Mater. 59 (2011) 1389–1399.

[39] N. Birks, G.H. Meier, F.S. Pettit, Introduction to the High Temperature Oxidation of Metals, Cambridge university press, 2006.

[40] S.C. Tsa, A.M. Huntz, J. Philibert, Diffusion of54Cr and18O in Cr2O 3 scales and growth mechanism, Defect Diffus. Forum 143 (1997) 1195–1200.

[41] B.A. PINT, Experimental observations in support of the dynamic-segregation theory to explain the reactive-element effect, Oxid. Met. 45 (1996) 1–37.

[42] P.Y. Hou, Y. Niu, C. Van Lienden, Analysis of pore formation at oxide–alloy interfaces—I: experimental results on FeAl, Oxid. Met. 59 (2003) 41–61.

[43] X.Y. Tan, F. Klein, A. Litnovsky, T. Wegener, J. Schmitz, C. Linsmeier, J.W. Coenen, U. Breuer, M. Rasinski, P. Li, L.M. Luo, Y.C. Wu, Evaluation of the high temperature oxidation of W-Cr-Zr self-passivating alloys, Corros. Sci. 147 (2019) 201–211.

[44] J. Liu, C. Tang, M. Steinbrück, J. Yang, U. Stegmaier, M. Große, Yun Di, H. J. Seifert, Transient experiments on oxidation and degradation of Cr-coated Zircaloy in steam up to 1600℃, Submitted to Corrosion Science (2021).

[45] X. Han, J. Xue, S. Peng, H. Zhang, An interesting oxidation phenomenon of Cr coatings on Zry-4 substrates in high temperature steam environment, Corros. Sci. 156 (2019) 117–124.

[46] X. Han, C. Chen, Y. Tan, W. Feng, S. Peng, H. Zhang, A systematic study of the oxidation behavior of Cr coatings on Zry4 substrates in high temperature steam environment, Corros. Sci. 174 (2020), 108826.

[47] Y.T. Cheng, W.L. Johnson, M.A. Nicolet, Dominant moving species in the formation of amorphous NiZr by solid-state reaction, Appl. Phys. Lett. 47 (1985) 800–802.

[48] S.B. Newcomb, K.N. Tu, Transmission electron microscopic observations of amorphous NiZr alloy formation by solid-state reaction, Appl. Phys. Lett. 48 (1986) 1436–1438.

[49] W. Xiang, S. Ying, Reaction Diffusion in chromium-zircaloy-2 System, China Nuclear Information Centre, 2001.

[50] S. Taniguchi, D.L. Carpenter, The influence of scale/metal interface characteristics on the oxidation behaviour of iron at elevated temperatures, Corros. Sci. 19 (1979) 15–26.

[51] M.W. Brumm, H.J. Grabke, Oxidation behaviour of NiAl—II. Cavity formation beneath the oxide scale on NiAl of different stoichiometries, Corros. Sci. 34 (1993) 547–561.

[52] H. Svensson, P. Knutsson, K. Stiller, Formation and healing of voids at the metal–Oxide interface in NiAl alloys, Oxid. Met. 71 (2009) 143–156.

[53] S. Perusin, B. Viguier, D. Monceau, L. Ressier, E. Andrieu, Injection of vacancies at metal grain boundaries during the oxidation of nickel, Acta Mater. 52 (2004) 5375–5380.

[54] Z. Wang, Y. Takeda, Amorphization and structural modification of the oxide film of Ni-based alloy by in-situ H charging in high temperature high pressure water environment, Corros. Sci. 166 (2020), 108474.

[55] C. Lemaignan, 2.07 – zirconium alloys: properties and characteristics, Comprehensive Nuclear Mater. (2012) 217–232.

[56] B. Hjorvarsson, A. Stierle, G. Song, H. Zabel, Hydrogen affinity at Cr/α–Cr2O3 metal/oxide interfaces studied by the 1H (15N, αγ) 12C nuclear resonance reaction, Vacuum. 52 (1999) 291–294.

[57] R.H. Bricknell, D.A. Woodford, The mechanism of cavity formation during high temperature oxidation of nickel, Acta Metall. 30 (1982) 257–264.

[58] B. Pieraggi, R.A. Rapp, Stress generation and vacancy annihilation during scale growth limited by cation-vacancy diffusion, Acta Metall. 36 (1988) 1281–1289.

[59] N. Birks, G.H. Meier, F.S. Pettit, Introduction to the High Temperature Oxidation of Metals, Cambridge university press, 2006, p. 77. Chapter 4.

[60] A.M. Huntz, Stresses in NiO, Cr2O3 and Al2O3 oxide scales, Mater. Sci. Eng. A 201 (1995) 211–228.

[61] X. Lu, Q. Hu, W. Yang, L. Bai, H. Sheng, L. Wang, F. Huang, J. Wen, D.J. Miller, Y. Zhao, Pressure-induced amorphization in single-crystal Ta2O5 nanowires: a kinetic mechanism and improved electrical conductivity, J. Am. Chem. Soc. 135 (2013) 13947–13953.

[62] N. Kawai, T. Atou, S. Ito, K. Yubuta, M. Kikuchi, K.G. Nakamura, K. Kondo, Aligned nanocrystalline fragmentation of mullite under shock loading, Adv. Mater. 19 (2007) 2375–2378.

[63] Y. Matsukawa, S. Kitayama, K. Murakami, Y. Shinohara, K. Yoshida, H. Maeno, H. L. Yang, T. Toyama, K. Yasuda, H. Watanabe, A. Kimura, H. Muta, S. Yamanaka, Y. F. Li, Y. Satoh, S. Kano, H. Abe, Reassessment of oxidation-induced amorphization and dissolution of Nb precipitates in Zr−Nb nuclear fuel cladding tubes, Acta Mater. 127 (2017) 153–164.